Volume 1 | Number 1 | Jan 2013 | Pages 1–100

Nanoscale

www.rsc.org/nanoscale

ROYAL SOCIETY OF CHEMISTRY

ROYAL SOCIETY OF CHEMISTRY

www.rsc.org/nanoscale

Journal Name

Dynamic Article Links ▶

ARTICLE TYPE

Ice-templated, pH-tunable self-assembly route to hierarchically porous graphene nanoscroll networks

Young-Eun Shin[a], Young Jin Sa[a], Seungyoung Park[a], Jiwon Lee[a], Kyung-Hee Shin[b], Sang Hoon Joo[a,*], and Hyunhyub Ko[a,*]

Porous graphene nanostructures are of great interest for applications in catalysts and energy storage devices. However, the fabrication of three-dimensional (3D) macroporous graphene nanostructures with controlled morphology, porosity and surface area still presents significant challenges. Here we introduce
10 an ice-templated self-assembly approach for the integration of two-dimensional graphene nanosheets into hierarchically porous graphene nanoscroll networks, where the morphology of porous structures can be easily controlled by varying the pH conditions during the ice-templated self-assembly process. We show that freeze-casting of reduced graphene oxide (rGO) solution results in the formation of 3D porous graphene microfoams below pH 8 and hierarchically porous graphene nanoscroll networks at pH 10. In
15 addition, we demonstrate that graphene nanoscroll networks show promising electrocatalytic activity for the oxygen reduction reaction (ORR).

Introduction

Graphenes have received great interest recently due to their intriguing physical, chemical, and mechanical properties.[1-6] In
20 particular, three-dimensional (3D) porous graphene structures have emerged as a key framework for applications in catalysts,[7, 8] sensors,[9-11] and energy storage devices.[12-17] However, integration of two-dimensional (2D) graphene sheets into 3D porous structures with controlled morphology, porosity and surface area
25 is a challenging task. Various strategies based on template-induced assembly of graphene sheets into 3D porous structures have been suggested. For example, colloid particles,[18, 19] bubbles,[20] metal forms,[21, 22] CNTs,[23, 24] and oil microdrops[25] have been utilized as templates for the fabrication of porous graphene
30 structures. Although these template-based methods provided efficient routes for the porous graphene structures, these methods require additional template etching process in strong solvents or acids, which may affects the final graphene surface chemistries and makes the process complicated. Recently, hydrothermal self-
35 assembly of graphene oxide (GO) or reduced GO (rGO) into 3D porous structures have been proposed as efficient template-less routes for the fabrication of monolithic porous graphene structures.[26-29] In this approach, graphene hydrogel with 3D porous structure is formed during the hydrothermal process and
40 the freeze-drying process is utilized for the transformation of graphene hydrogel into aerogel by solvent sublimation. However, the self-assembly of graphene has limitation in the formation of tunable structures with various pore sizes and morphologies.

Freeze-casting or ice-templating strategy has attracted
45 considerable attention as a versatile, environmentally benign, and inexpensive method to crystallize suspensions of ceramic colloids, polymers, and composite mixtures into a variety of 3D porous structures.[30-32] In this method, when a liquid suspension freezes, the particles are rejected from the growing ice crystal and
50 subsequently accumulated between the ice crystals. This segregation behavior increases the particle concentration and promotes the interparticle interactions, resulting in the directed-assembly of particles between the ice crystals. Subsequent high-vacuum sublimation of ice crystal structure leads to the 3D
55 porous structure which is pre-defined by the morphology of ice crystal. Recently, this technique is successfully exploited for the formation of 3D carbon nanostructures including graphene and carbon nanotubes.[33-36] However, few reports have focused on the controlled self-assembly of graphene during the ice-templating
60 process although the unique 2D geometry and surface functional groups of GO or rGO are expected to have a critical role in the self-assembly of graphene when they are concentrated and confined between the ice crystals. The shape or conformation of single-atom-thick 2D graphene layer has been known to be
65 vulnerable to physicochemical environmental conditions (pH, solvent, temperature, geometrical confinement, etc.), leading to conformational changes including folding, bending, and scrolling behaviors.[37-42] Hence, the combination of graphene self-assembly with the ice-templating process may provide a route for the
70 deterministic control of graphene morphology via simple, low-cost, and large quantity solution process.

Here, we present a facile approach for the fabrication of macroporous graphene nanoscrolls and graphene microfoams using ice-segregation induced self-assembly of 2D rGO at

different pH conditions during freeze-casting process. In this method, freezing process increase the rGO concentration between the ice crystals and provide the geometrical confinement for the self-assembly of rGO. In addition, protonation and deprotonation of carboxylic group at the edge of rGO at different pH conditions is exploited to tune the electrostatic interactions. Therefore, the highly concentrated rGO with controllable electrostatic interactions leads to the unique self-assembly behavior of rGO.
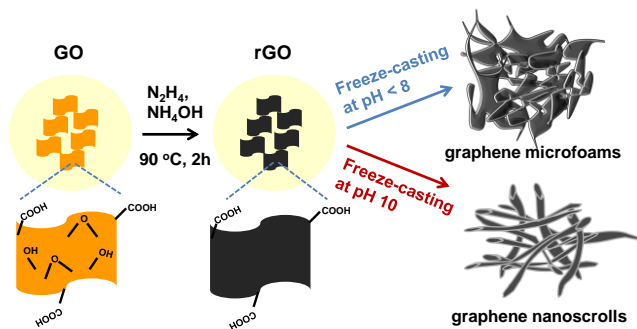

Figure 1. Ice-templated self-assembly of rGO sheets into hierarchically porous graphene nanoscroll networks and microfoams depending on pH values. Most of functional groups except for carboxyl groups on GO are reduced after hydrazine reduction. Residual carboxyl groups are critical factors for the formation of different morphology depending on pH conditions. Freeze-casting of rGO results in the formation of graphene nanoscrolls at pH 10 and graphene microfoams below pH 8.

Figure 1 shows the schematic procedure for the formation of graphene nanoscrolls and microfoams. In this process, the aqueous GO suspension is reduced with hydrazine, removing hydroxyl and epoxide groups on the basal plane of GO. The carboxylic groups at the edge of GO is maintained after the reduction process since the hydrazine does not reduce the carboxylic groups on GO sheets.[43] The carboxylic group at the edge of rGO is protonated below pH 8 and deprotonated at pH 10, affecting the electrostatic interactions between the rGO sheets. Then, freeze-casting of rGO solution results in the formation of 3D porous graphene foams below pH 8 and graphene nanoscrolls at pH 10. We also demonstrate that the 3D rGO-based nanostructures show promising electrocatalytic activity for the oxygen reduction reaction (ORR).

Experimental

Synthesis of graphene oxide

Graphene oxide was prepared using modified hummers method.[44,45] Briefly, graphite powder (SP-1, Bay Carbon), $K_2S_2O_8$ (Sigma Aldrich), and P_2O_5 (Sigma Aldrich) were added to concentrated H_2SO_4 solution (Sigma Aldrich). This solution was heated using 80 ^{o}C oil bath for 4.5 hours with vigorous stirring. Then, the solution was carefully diluted with de-ionized (DI) water, followed by vacuum filtration and additional DI washing to make the pH of solution neutral. The filtrate was dried in a 30 ^{o}C vacuum oven overnight. The pre-oxidized graphite was then added to concentrated H_2SO_4 in an ice bath. Then, $KMnO_4$ (Sigma Aldrich) was slowly added to the solution under vigorous stirring while maintaining the solution temperature below 20 ^{o}C, and the solution was stirred at 36 ^{o}C for 2 hours. The mixture was gradually diluted using DI water in an ice bath while maintaining

the temperature below 50 ^{o}C. Next, the mixture was heated at 35 ^{o}C for 2 hours and diluted with copious amounts of DI water. Subsequently, 30 % H_2O_2 (Sigma Aldrich) was added to this mixture, resulting in the color change into bright yellow with violent bubbles. This mixture was stirred for 1 hour, centrifuged for several times with 10 % HCl to remove residual salts, and subjected to dialysis to adjust the acidity. Finally, the resulting solution was concentrated, dried in vacuum oven at 30 ^{o}C, and re-dispersed in DI water by sonication to achieve GO solution.

Synthesis of graphene nanoscrolls

Graphene oxide was reduced using hydrazine monohydrate (35 wt% in water, Sigma Aldrich).[46] The obtained brown GO solution was centrifuged with 4000 rpm for 10 min to remove any unexfoliated graphite oxide. Then, hydrazine monohydrate and ammonia solution (28 wt% in water) were added to the graphene oxide solution (0.5 mg/ml), and the mixture was heated at 90 ^{o}C for 2 hours. The color of solution changed from brown to black as the reduction proceeded. After cooling to room temperature, porous graphene nanoscrolls were fabricated using pH control and freeze-casting process. For these processes, the rGO dispersion was adjusted from pH 2 to pH 12 using HCl and NH$_4$OH solution, followed by centrifugation, supernatant removal, and freezing with liquid nitrogen. Finally, the rGO aerogel was achieved after lyophilisation for several days. The rGO aerogel was further reduced by thermal annealing at 600 oC for 1 hour in Ar atmosphere.

Characterization of GO and rGO

The morphology and thickness of graphene oxides was analyzed using Atomic Force Microscope (AFM, Dimension 3000, Veeco, USA). The chemical functional groups of GO and rGO were analyzed using confocal Raman microscope (alpha 300R, WITec, Germany), UV-vis Spectrophotometer (JASCO, Japan), X-ray Photoelectron Spectroscopy (XPS, K-alpha, Thermo Fisher, UK). The charge density of rGO solution was verified by zeta potential measuring system (Nano ZS, Malvern, UK). The morphology of porous graphene structure was characterized by field emission scanning electron microscope (FE-SEM, S-4800, Hitachi, Japan) and transmission electron microscope (TEM, JEM-2100, JEOL, Japan). The textural properties of the samples were investigated by nitrogen physisorption analyzer (BELSORP-MAX system, BEL, Japan). Before measurements, the sample was evacuated under vacuum ($< 10^{-5}$ Pa) at room temperature for 5 h. Total pore volume was determined at the relative pressure of 0.98-0.99. Specific surface area was calculated by Brunauer-Emmett-Teller (BET) equation at the relative pressure range of 0.05-0.30.

Electrochemical Measurements

The electrochemical characterization was carried out using an IviumStat electrochemical analyzer. The electrochemical measurements were conducted at room temperature using a three-compartment electrochemical cell. A graphite rod and Hg/HgO were used as counter and reference electrodes, respectively. All data were reported in the reversible hydrogen electrode (RHE) potential scale. The calibration of Hg/HgO reference electrode with respect to the RHE was carried out as follows. The Hg/HgO and RHE (HydroFlex) were used as reference and working electrodes, respectively, and immersed in N$_2$-saturated 0.1 M

KOH (99.999%, Aldrich) for at least 30 min. Then, constant open circuit potential (calibration value) was obtained. RHE calibration of Ag/AgCl reference electrode was also conducted in the same manner for comparison of ORR activity with previous reports 5 (Table S2). The catalyst ink was prepared by sonication (30 min) of mixture composed of 3 mg catalyst, 200 µL H₂O, 60 µL Nafion (5 wt% in isopropanol, Aldrich), and 940 µL ethanol (99.9%, Samchun). The ink (3 µL) was coated on a glassy carbon (GC) electrode (4 mm in diameter) in rotating disk electrode 10 (RDE), and dried by rotating the RDE at 700 rpm. The resulting catalyst loading was 60 µg cm⁻². The RDE was polished with 1.0 µm and 0.3 µm alumina suspension to generate mirror-like GC surface.

Before the ORR activity measurement, the catalyst surface was 15 electrochemically cleaned by cycling potential in a range from 0.05 to 1.20 V (vs. RHE) for 50 times at a scan rate of 100 mV s⁻¹ in N₂-saturated 0.1 M KOH. Subsequently, cyclic voltammetry (CV) curve was obtained in the same potential range, but with different scan rate of 20 mV s⁻¹. The ORR activity of the catalyst 20 was measured in a potential profile (1.1 → 0.2 → 1.1 V (vs. RHE)) at a scan rate of 5 mV s⁻¹ with O₂ gas bubbling, and with electrode rotation speeds of 1600, 1225, 900, 625, and 400 rpm. The cathodic and anodic currents were averaged for capacitive current correction.[47] The kinetic current was calculated by using 25 the Koutecky-Levich equation.

$$\frac{1}{i} = \frac{1}{i_k} + \frac{1}{i_d}$$

Here, i, i_k, and i_d are the measured current, kinetic current, and diffusion-limited current, respectively.[48]

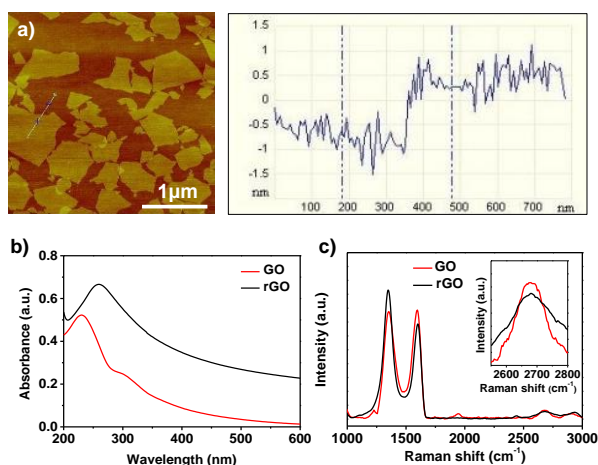## Results and Discussion

30

Figure 2. AFM, UV-vis absorbance, and Raman scattering of GO and rGO. (a) AFM image of GO; the thickness and width of GO sheet is ~1 nm and below ~1 µm, (b) UV-vis absorbance spectra of GO and rGO; red-shift 35 of absorbance spectra appears after the hydrazine reduction, (c) Raman spectra of GO and rGO with increased I_D/I_G ratio.

The AFM image of typical GO sheets shows the well-exfoliated single-layer GO sheets with thickness of ~1 nm and the lateral size below ~1 µm. (Figure 2a). The UV-vis absorption of GO 40 solution shows a peak at ~231 nm, which is attributed to the π →

π* transitions of aromatic C–C bonds, and also a shoulder peak at ~300 nm due to the $n \rightarrow \pi^*$ transitions of C=O bonds.[49] When GO is reduced to rGO using hydrazine, the peak from aromatic C–C bonds shows a red-shift from 231 nm to 270 nm (Figure 2b), 45 which is attributed to the restoration of π-electron conjugation.[50] The structural change after the reduction of graphene is also observed from Raman analysis. Raman spectrum of GO sheets shows a G peak at 1594 cm⁻¹ and a D peak at 1353 cm⁻¹. These G and D peaks are also observed in rGO, but shifted to 1600 cm⁻¹ 50 for G peak and 1349 cm⁻¹ for D peak. In addition, the ratio of D to G peaks increased from 0.96 to 1.32 after the reduction process (Figure 2c), which has been attributed to the decrease of average size of sp² domain due to the increase of the number of small size sp² domain after reduction. [51-54] We also observe 2D peaks of GO 55 and rGO at 2680 cm⁻¹, which are consistent with the 2D Raman peak of single layer graphene sheet.[55, 56]
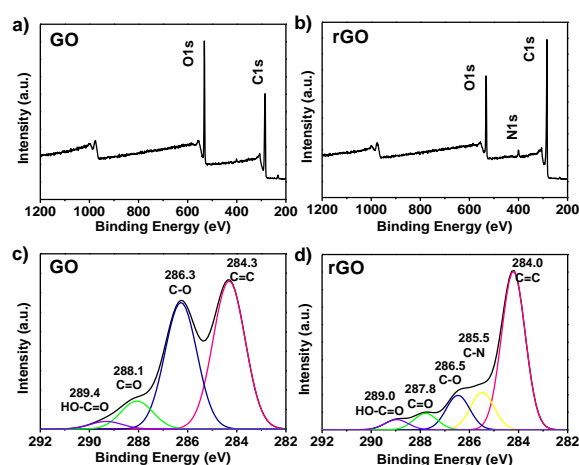

Figure 3. XPS spectra of GO and rGO. (a) and (b) wide region of XPS spectra: C1s, O1s peaks commonly appear, and N1s peak appear after 60 the hydrazine reduction; (c) and (d) C1s region of XPS spectra: Commonly 4 spectra related to graphitic C=C and functional groups (C-O, C=O, HO-C=O) appear in GO and rGO. Especially in rGO, additional peak with C-N appears due to the use of hydrazine during the reduction process.

Figure 3a and b presents survey XPS spectra of GO and rGO 65 sheets. After reduction, the C/O ratio was remarkably increased due to the removal of oxygen containing functional groups. The appearance of N1s peak after reduction (Figure 3b) can be attributed to the nitrogen doping by hydrazine monohydrate during reduction process.[57] The C1s XPS spectrum of GO (Figure 70 3c) indicates the degree of oxidation with four components which correspond to C atoms in different functional groups; the non-oxygenated ring C=C at 284.3 eV, the C atom in C-O bond at 286.3 eV, the carbonyl C (C=O) at 288.1 eV, and the carboxylate carbon (HO-C=O) at 289.4 eV. The C1s XPS spectrum of rGO 75 (Figure 3d) showed the similar functional groups, but with decreased intensities and shifted peak positions in the oxygen-containing groups. On the other hand, the increase of C=C bond peak and the appearance of additional C=N bond peak after the reduction process indicate that hydrazine reduction causes the 80 restoration of sp² networks on the basal plane and the formation of pyrazole (C₃H₃N₂H) which induces the nitrogen-doping.[57] The above XPS analysis indicates that most of oxygen-containing functional groups are removed, resulting in the increase of sp²

networks in the basal plane of rGO. These changes of chemical functionalities decrease the stability of rGO sheets in aqueous solution, increasing the tendency of agglomeration of rGO sheets with each other. However, rGO could be well dispersed in high pH solution since carboxylic groups at the edge of rGO sheets can be deprotonated to provide repulsive charges. It has been reported that the hydrazine could not reduce the carboxylic groups at the edge of GO sheets.[43]
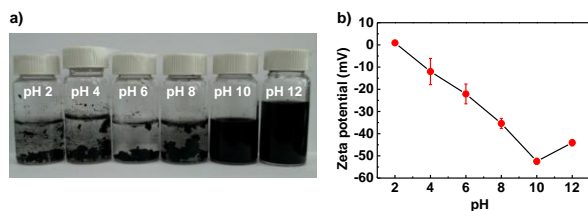
epoxide, hydroxyl groups on the basal planes and carboxylic groups at the edges, resulting in stable dispersion of aqueous GO solution.[58] Most of functional groups are removed after chemical reduction with hydrazine, but carboxyl groups are unlikely to be removed as can be seen in Figure 3. The remaining carboxyl groups at the edges of rGO sheets are critical to disperse rGO sheets in high pH solution (Figure 4a).[46] Figure 4b shows zeta potential values of rGO depending on pH of solution. The zeta potential decreases with the increase of the pH values due to the charge build-up caused by the ionization of carboxylic groups at the edge of rGO. The charge density of rGO sheets decreased with the increase of pH values and was the highest (-52 mV) at pH 10. Carboxyl groups at the edges of rGO sheets are deprotonated at high pH values, resulting in more negatively charged rGO sheets and stronger electrostatic repulsion between rGO sheets. As a result, rGO sheets with high charge density could be stable inside the aqueous solution even after reduction. However, when the pH value is 12, the zeta potential of rGO dispersion increased, decreasing the stability of rGO solution. This decreased stability of rGO solution at pH 12 can be attributed to the compression of the double layer at high ionic strengths.[43] Since the rGO dispersion is not stable when the zeta potential is higher than −30 mV, the rGO solution shows aggregated behavior for pH values below pH 8.
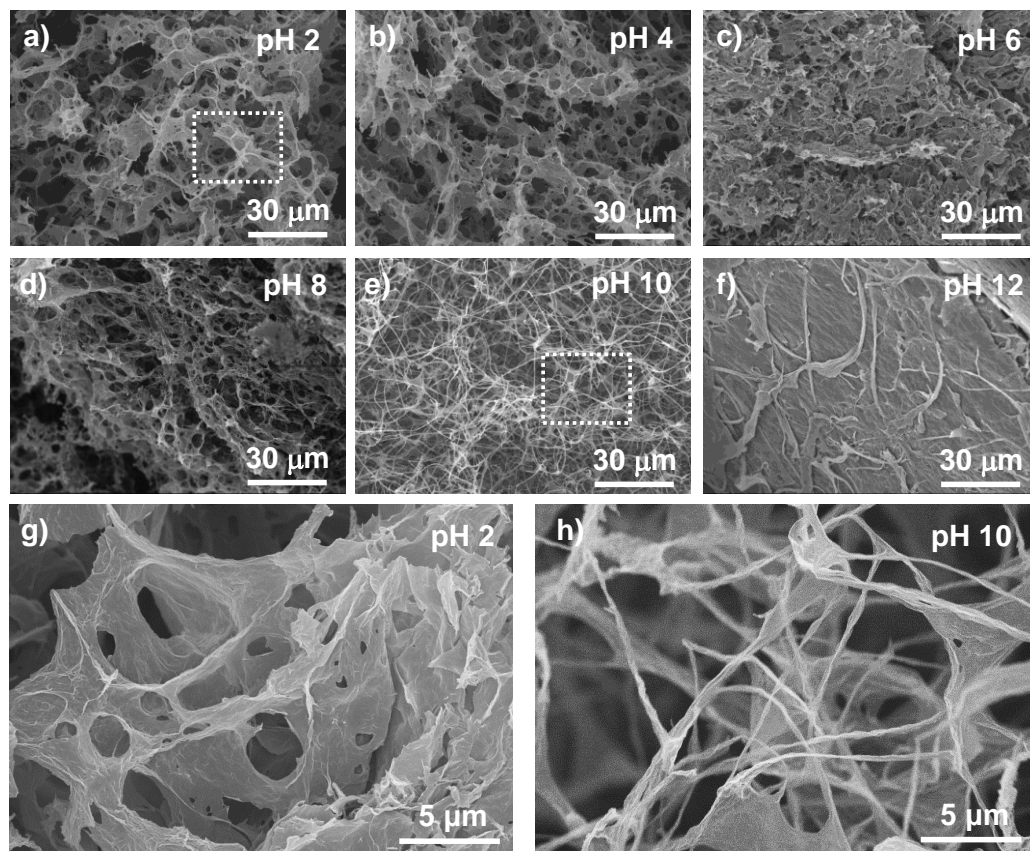

Figure 4. **Stability of rGO solution depending on the pH conditions**. Change of rGO dispersion as pH conditions change from 2 to 12. (a) rGO aggregates are precipitated for solution pH below 8. Stable rGO solution is observed for solution pH over 10. (b) Zeta potential analysis of rGO dispersion at different pH values; rGO solution at pH 10 shows the largest charge density.

The stability of rGO solution at different pH values can be analyzed via zeta potential measurements of rGO dispersion (Figure 4). GO sheets have a rich variety of functional groups like

Figure 5. SEM images of different morphologies of porous rGO structures. Porous rGO structures are fabricated by ice-templated self-assembly of rGO sheets at different pH values.(a)-(f) pH values of 2, 4, 6, 8, 10, and 12 in alphabetical order. The morphology of porous rGO structures depend on pH conditions with dendrite-like microfoams below pH 8 and wire-like nanoscrolls at pH 10. (g) and (h) high-resolution SEM images of porous rGO structures formed at pH 2 and 10.

ARTICLE TYPE

Figure 5 presents SEM images of self-assembled rGO architectures after freeze-casting of rGO solution at different pH conditions. When the pH of rGO solution is below 8, 2D rGO sheets are aggregated into stacked layers which are connected 5 with each other, resulting in the formation of porous rGO microfoams (Figure 5a-d, g). On the other hand, rGO sheets were self-assembled into wire-like graphene nanoscrolls forming macroporous networks at pH 10 condition (Figure 5e, h). When the pH value is 12, rGO sheets are stacked into thick multilayers 10 without porous structures (Figure 5f). These different morphologies of rGO sheets after freeze-casting of rGO solution at different pH conditions can be attributed to the stability of rGO sheets in aqueous solution at different pH values when they are physically confined between the growing ice crystals.

15 At low pH, carboxylic groups at the edge of rGO sheets are protonated, resulting in the decrease of electrostatic repulsions and the increase of van der Waals or π-π interactions between rGO sheets,[39] which induce stacking of rGO sheets into thick multilayer sheets. The stacking of rGO sheets leads to the 20 precipitation of rGO sheets at low pH condition (Figure 4a). The subsequent freeze-casting process results in the formation of porous structures of stacked rGO sheets, where the microscale pore diameter is determined by the size of ice crystals. The ice crystal-induced formation of microscale (5-15 μm) pores can be 25 also observed for high density GO solution when they go through a freeze-casting process (Figure S1), where microscale honeycomb structures of GO sheets are formed, which has been attributed to the formation of ice crystals during the freeze-casting process in the previous report.[59] At pH 10 condition, 30 carboxylic groups at the edge of rGO sheets are deprotonated and charged, leading to the electrostatic repulsions between rGO sheets and the well-dispersed rGO solution. As contrary to the stacked rGO sheets at low pH, well-dispersed single-layer rGO sheets at pH 10 have a tendency to be rolled up into graphene 35 nanoscrolls during the freeze-casting process, which results in the network formation of graphene nanoscrolls.

The mechanism for the formation of graphene nanoscrolls can be explained as follows. During the freeze-casting process, the growing ice-crystal drives the transport and removal of water 40 stabilizing the deprotonated rGO, resulting in the increase of surface stress of rGO sheet. Then, the destabilized rGO tends to undergo conformational change into more stable forms by twisting, bending, and rolling. When one part of basal plane overlaps another part of basal plane within the rGO during the 45 conformational change, the π-π interaction between basal planes of rGO decreases the surface stress and stabilizes the rGO.[42]

Figure 6a shows the schematic representation of the formation mechanism of graphene nanoscrolls. The conformational change of rGO sheets into nanoscrolls via twisting, bending, and rolling 50 resulted in crumpled nanoscrolls, as can be seen in Figure 6b-d with SEM and TEM images. The crumpled nanoscrolls are more

clearly observed when large size rGO (~4 μm) sheets are used in the formation of graphene nanoscrolls (Figure S4) because the low bending rigidity of large size rGO sheets facilitates the 55 conformational change of rGO sheets. The nanoscroll formation is spontaneous. The freeze-casting process at lower growth rate of ice crystals did not result in the formation of graphene nanoscrolls. As can be seen in Figure S2, stacked multilayer graphene sheets were observed when we slowly freeze the rGO 60 solution in the refrigerator and freeze-drying. The freeze-casting of GO solution at different pH conditions resulted in various morphologies different from those of rGO architectures. As can be seen in Figure S3, at low pH, GO crumpled into micrometer scale particles without stacking together. At pH 10, GO tends to 65 form mostly twisted and self-folded structures with only small portions of rolled structures. The morphologies of GO different from rGO structures can be attributed to the lower π-π interactions between GO sheets compared to the rGO.
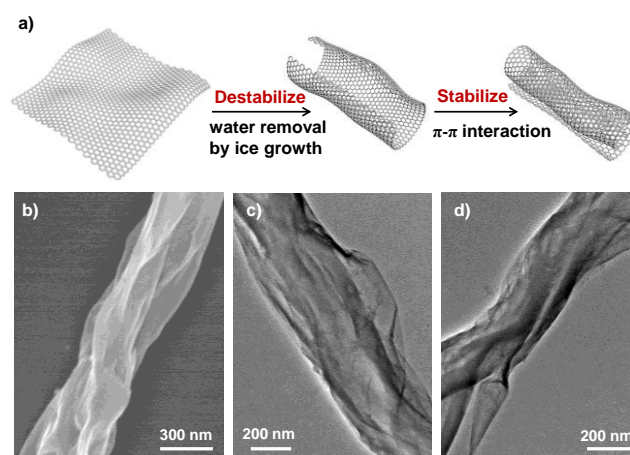
70 **Figure 6. Formation of graphene nanoscrolls.** (a) Formation mechanism of rGO nanoscrolls during the ice-templated self-assembly process; the st abilized rGO at pH 10 become destabilized by the water removal surroun ding the rGO sheets during the freeze-casting process, resulting in graphe ne bending and folding, and finally nanoscrolls which are stabilized by π-
75 π interactions. (b) SEM and (c), (d) TEM images of graphene nanoscrolls..

The porous and textural properties of the 3D nanostructures assembled from GO and rGO at pH 6 and 10 were analyzed by nitrogen adsorption-desorption isotherms (Figure 7). The all four isotherms showed a nitrogen uptake at high relative pressure 80 above 0.9. In particular, rGO-driven nanoscrolls assembled at pH 10 (rGO-pH10) featured fairly pronounced uptake of nitrogen in the relative pressure range of 0.9~1.0 of the isotherm. This indicates that the rGO-pH10 sample has considerable amount of macropores contained within nanoscroll structures. In contrast, 85 the GO-pH10 sample showed relatively small nitrogen uptake, compared to the rGO-pH10, as it has only small portion of rolled structure (Figure S3e). The four samples had BET surface areas in the range of 50 to 110 m^2 g^{-1}, with the rGO-pH10 sample

Nanoscale Accepted Manuscript

exhibiting the highest area of 110 m^2 g^{-1} (Table S1). Although these values of surface areas are lower than those of rGO films or aerogels, the ORR activity exhibited superior or comparable results,[60, 61] indicating the critical role of rGO nanoscrolls in the electrocatalytic activity.
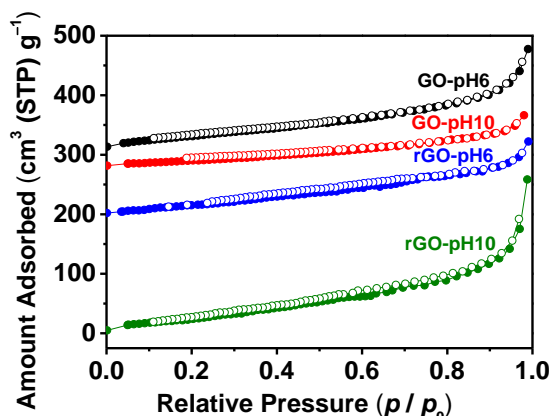

Figure 7. Nitrogen adsorption-desorption isotherms. Nitrogen physisorption isotherms of the samples obtained at 77 K. The isotherms of the rGO-pH6, GO-pH10, and GO-pH6 were offset by 200, 280, and 310 cm^3 g^{-1}, respectively.

The electrochemical property and ORR activity of the graphene nanostructures were investigated in an alkaline solution (0.1 M KOH) using RDE. Figure 8a shows cyclic voltammetry (CV) curve of the samples measured in N$_2$-saturated 0.1 M KOH at a potential scan rate of 20 mV s^{-1}. The CV curves clearly reveal that the rGO samples exhibit higher current densities than the GO samples, indicating that the rGO-driven nanostructures have relatively higher portion of electrochemically active areas. To compare the ORR activity of the samples, CV measurement was conducted in O$_2$-saturated electrolyte with RDE rotation of 1600 rpm (Figure 8b). Polarization curves in Figure 8b were obtained after averaging cathodic and anodic currents for capacitive-current correction. The rGO samples have higher onset potential around 0.82 V (vs. RHE) and diffusion-limited current than the GO samples. This trend of activity order was in accordance with active areas obtained with CVs (Figure 8a). Specifically, GO-pH6 and rGO-pH10 have better ORR activity than GO-pH10 and rGO-pH6, respectively, and this can be attributed to higher BET surface area (Table S1).
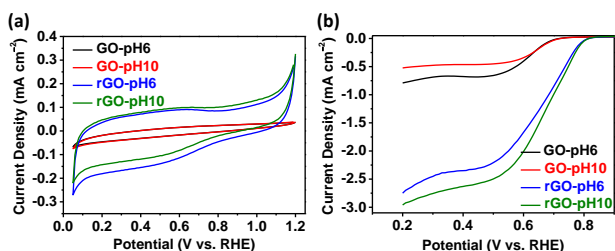

Figure 8. Electrochemical analyses. (a) Cyclic voltammetry (CV) curve of the samples measured in N$_2$-saturated 0.1 M KOH at a scan rate of 20 mV s^{-1} (b) Polarization curves of the samples after averaging cathodic and anodic currents of CV data obtained in O$_2$-saturated electrolyte at a scan rate of 5 mV s^{-1} and RDE rotation speed of 1600 rpm.

The better ORR activity of rGO samples than that of GO

samples results from chemical and thermal removal of oxygen-functional groups located on the GO sheets which hamper electrical conduction, leading to recovery of C-C sp^2 network and electron conductivity. Furthermore, the use of hydrazine and ammonium hydroxide and subsequent thermal annealing rendered the formation of nitrogen groups on the rGO samples, which could further enhance their activity towards the ORR. We point out that the ORR activity of the rGO-pH10 is superior to or on a par with those of previously reported N-doped graphene nanostructures (Table S2). The high ORR activity of the rGO-pH10 could be in part due to the twisted, bent, and rolled surface of the rGO-pH10, which possibly has higher strain compared to the smooth counterpart, facilitating O-O bond activation and enhance ORR kinetics.

Conclusions

In conclusion, we employed an ice-templating approach for the pH-tunable self-assembly of 2D graphene sheets into 3D macroporous graphene nanoscroll networks. During the freeze-casting of graphene solution, the geometrical confinement by the growing ice crystal and the intermolecular interactions depending on pH conditions allowed the easy control of morphology and surface area of porous graphene nanostructures. This approach does not require any traditional sacrificial templates for the formation of 3D porous structures, thus simplifying the fabrication process without the need of complicated template etching step in strong solvents and acids. Although this approach has been applied only to graphene in this study, it can be potentially expanded to other nanotubes and nanoparticles for their pH-tunable self-assembly into controlled porous nanostructures. The 3D macroporous graphene nanoscroll networks with enhanced catalytic activity compared to graphene microfoams may find numerous applications in catalysts, sensors, and energy storage devices

Notes and references

a *School of Energy and Chemical Engineering, KIER-UNIST Advanced Center for Energy, Ulsan National Institute of Science and Technology (UNIST), Ulsan Metropolitan City, 689-798, Republic of Korea. E-mail: shjoo@unist.ac.kr, hyunhko@unist.ac.kr*
b *New and Renewable Energy Research Division, Korea Institute of Energy Research (KIER), Daejeon 305-343, Republic of Korea*
† Electronic Supplementary Information (ESI) available: [details of any supplementary information available should be included here]. See DOI: 10.1039/b000000x/

1. A. K. Geim and K. S. Novoselov, *Nature Mater.*, 2007, **6**, 183-191.
2. K. Novoselov, A. Geim, S. Morozov, D. Jiang, M. I. K. I. V. Grigorieva, S. Dubonos and A. Firsov, *Nature*, 2005, **438**, 197-200.
3. K. Novoselov, A. Geim, S. Morozov, D. Jiang, Y. Zhang, S. Dubonos, I. Grigorieva and A. Firsov, *Science*, 2004, **306**, 666-669.
4. K. I. Bolotin, K. J. Sikes, Z. Jiang, M. Klima, G. Fudenberg, J. Hone, P. Kim and H. L. Stormer, *Solid State Commun.*, 2008, **146**, 351-355.

5. C. Lee, X. Wei, J. W. Kysar and J. Hone, *Science*, 2008, **321**, 385-388.
6. S. Morozov, K. Novoselov, M. Katsnelson, F. Schedin, D. Elias, J. Jaszczak and A. Geim, *Phys. Rev. Lett.*, 2008, **100**, 16602.
7. X. Li, W. Cai, J. An, S. Kim, J. Nah, D. Yang, R. Piner, A. Velamakanni, I. Jung and E. Tutuc, *Science*, 2009, **324**, 1312-1314.
8. Z. Tang, S. Shen, J. Zhuang and X. Wang, *Angew. Chem.*, 2010, **122**, 4707-4711.
9. J. D. Fowler, M. J. Allen, V. C. Tung, Y. Yang, R. B. Kaner and B. H. Weiller, *ACS Nano*, 2009, **3**, 301-306.
10. F. Schedin, A. Geim, S. Morozov, E. Hill, P. Blake, M. Katsnelson and K. Novoselov, *Nature Mater.*, 2007, **6**, 652-655.
11. Y. Shao, J. Wang, H. Wu, J. Liu, I. A. Aksay and Y. Lin, *Electroanalysis*, 2010, **22**, 1027-1036.
12. G. Eda, G. Fanchini and M. Chhowalla, *Nature Nanotechnol.*, 2008, **3**, 270-274.
13. S. R. C. Vivekchand, C. S. Rout, K. Subrahmanyam, A. Govindaraj and C. N. R. Rao, *J. Chem. Sci.*, 2008, **120**, 9-13.
14. A. Vollmer, X. Feng, X. Wang, L. Zhi, K. Müllen, N. Koch and J. Rabe, *Applied Physics A: Materials Science & Processing*, 2009, **94**, 1-4.
15. X. Wang, L. Zhi and K. Müllen, *Nano Lett.*, 2008, **8**, 323-327.
16. M. A. Worsley, P. J. Pauzauskie, T. Y. Olson, J. Biener, J. H. Satcher Jr and T. F. Baumann, *J. Am. Chem. Soc.*, 2010, **132**, 14067-14069.
17. E. J. Yoo, J. Kim, E. Hosono, H. Zhou, T. Kudo and I. Honma, *Nano Lett.*, 2008, **8**, 2277-2282.
18. B. G. Choi, M. H. Yang, W. H. Hong, J. W. Choi and Y. S. Huh, *ACS Nano*, 2012, **6**, 4020-4028.
19. X. Huang, K. Qian, J. Yang, J. Zhang, L. Li, C. Yu and D. Zhao, *Adv. Mater.*, 2012, **24**, 4419-4423.
20. J. Xiao, D. Mei, X. Li, W. Xu, D. Wang, G. L. Graff, W. D. Bennett, Z. Nie, L. V. Saraf and I. A. Aksay, *Nano Lett.*, 2011, **11**, 5071-5078.
21. Z. Chen, W. Ren, L. Gao, B. Liu, S. Pei and H. M. Cheng, *Nature Mater.*, 2011, **10**, 424-428.
22. H. Ji, L. Zhang, M. T. Pettes, H. Li, S. Chen, L. Shi, R. Piner and R. S. Ruoff, *Nano Lett.*, 2012, **12**, 2446-2451.
23. K. H. Kim, Y. Oh and M. Islam, *Nature nanotechnol.*, 2012, **7**, 562-566.
24. S.-Y. Yang, K.-H. Chang, H.-W. Tien, Y.-F. Lee, S.-M. Li, Y.-S. Wang, J.-Y. Wang, C.-C. M. Ma and C.-C. Hu, *J. Mater. Chem.*, 2011, **21**, 2374-2380.
25. F. Zhang, X. Zhang, Y. Dong and L. Wang, *J. Mater. Chem.*, 2012, **22**, 11452-11454
26. Y. Xu, K. Sheng, C. Li and G. Shi, *ACS Nano*, 2010, **4**, 4324-4330.
27. H.-P. Cong, X.-C. Ren, P. Wang and S.-H. Yu, *ACS Nano*, 2012, **6**, 2693-2703.
28. P. Chen, J.-J. Yang, S.-S. Li, Z. Wang, T.-Y. Xiao, Y.-H. Qian and S.-H. Yu, *Nano Energy*, 2012, **2**, 249-256.
29. Z.-S. Wu, S. Yang, Y. Sun, K. Parvez, X. Feng and K. Müllen, *J. Am. Chem. Soc.*, 2012, **134**, 9082-9085.
30. S. Deville, E. Saiz, R. K. Nalla and A. P. Tomsia, *Science*, 2006, **311**, 515-518.
31. H. F. Zhang, I. Hussain, M. Brust, M. F. Butler, S. P. Rannard and A. I. Cooper, *Nature Mater.*, 2005, **4**, 787-793.
32. S. Deville, *Adv. Eng. Mater.*, 2008, **10**, 155-169.
33. L. Qiu, J. Z. Liu, S. L. Y. Chang, Y. Z. Wu and D. Li, *Nature Commun.*, 2012, **3**, 1241.
34. J. H. Zou, J. H. Liu, A. S. Karakoti, A. Kumar, D. Joung, Q. A. Li, S. I. Khondaker, S. Seal and L. Zhai, *ACS Nano*, 2010, **4**, 7293-7302.
35. L. Estevez, A. Kelarakis, Q. M. Gong, E. H. Da'as and E. P. Giannelis, *J. Am. Chem. Soc.*, 2011, **133**, 6122-6125.
36. J. L. Vickery, A. J. Patil and S. Mann, *Adv. Mater.*, 2009, **21**, 2180-2184.
37. L. M. Viculis, J. J. Mack and R. B. Kaner, *Science*, 2003, **299**, 1361-1361.
38. Z. P. Xu and M. J. Buehler, *ACS Nano*, 2010, **4**, 3869-3876.
39. R. L. D. Whitby, V. M. Gun'ko, A. Korobeinyk, R. Busquets, A. B. Cundy, K. Laszlo, J. Skubiszewska-Zieba, R. Leboda, E. Tombacz, I. Y. Toth, K. Kovacs and S. V. Mikhalovsky, *ACS Nano*, 2012, **6**, 3967-3973.
40. M. Quintana, M. Grzelczak, K. Spyrou, M. Calvaresi, S. Bals, B. Kooi, G. Van Tendeloo, P. Rudolf, F. Zerbetto and M. Prato, *J. Am. Chem. Soc.*, 2012, **134**, 13310-13315.
41. T. Sharifi, E. Gracia-Espino, H. R. Barzegar, X. E. Jia, F. Nitze, G. Z. Hu, P. Nordblad, C. W. Tai and T. Wagberg, *Nature Commun.*, 2013, **4**, 2319.
42. X. Xie, L. Ju, X. F. Feng, Y. H. Sun, R. F. Zhou, K. Liu, S. S. Fan, Q. L. Li and K. L. Jiang, *Nano Lett.*, 2009, **9**, 2565-2570.
43. B. Konkena and S. Vasudevan, *J. Phys. Chem. Lett.*, 2012, **3**, 867-872.
44. W. S. Hummers and R. E. Offeman, *J. Am. Chem. Soc.*, 1958, **80**, 1339-1339.
45. Y. Xu, H. Bai, G. Lu, C. Li and G. Shi, *J. Am. Chem. Soc.*, 2008, **130**, 5856-5857.
46. D. Li, M. B. Müller, S. Gilje, R. B. Kaner and G. G. Wallace, *Nature Nanotechnol.*, 2008, **3**, 101-105.
47. J. Suntivich, H. A. Gasteiger, N. Yabuuchi and Y. Shao-Horn, *J. Electrochem. Soc.*, 2010, **157**, B1263-B1268.
48. A. J. Bard and L. R. Faulkner, *Electrochemical Methods. Fundamentals and Applications., John Wiley & Sons, Inc*, 2001.
49. J. I. Paredes, S. Villar-Rodil, A. Martinez-Alonso and J. M. D. Tascon, *Langmuir*, 2008, **24**, 10560-10564.
50. D. Li, M. B. Muller, S. Gilje, R. B. Kaner and G. G. Wallace, *Nature Nanotechnol.*, 2008, **3**, 101-105.
51. S. Stankovich, D. A. Dikin, R. D. Piner, K. A. Kohlhaas, A. Kleinhammes, Y. Jia, Y. Wu, S. T. Nguyen and R. S. Ruoff, *Carbon*, 2007, **45**, 1558-1565.
52. V. C. Tung, M. J. Allen, Y. Yang and R. B. Kaner, *Nature Nanotechnol.*, 2008, **4**, 25-29.
53. J. Paredes, S. Villar-Rodil, P. Solis-Fernandez, A. Martinez-Alonso and J. Tascon, *Langmuir*, 2009, **25**, 5957-5968.
54. G. Eda and M. Chhowalla, *Advanced Mater.*, 2010, **22**, 2392-2415.
55. A. C. Ferrari, J. C. Meyer, V. Scardaci, C. Casiraghi, M. Lazzeri, F. Mauri, S. Piscanec, D. Jiang, K. S. Novoselov, S. Roth and A. K. Geim, *Phys. Rev. Lett.*, 2006, **97**.
56. K. Liu, J.-J. Zhang, F.-F. Cheng, T.-T. Zheng, C. Wang and J.-J. Zhu, *J. Mater. Chem.*, 2011, **21**, 12034.
57. S. Park, Y. Hu, J. O. Hwang, E.-S. Lee, L. B. Casabianca, W. Cai, J. R. Potts, H.-W. Ha, S. Chen and J. Oh, *Nature Commun.*, 2012, **3**, 638.
58. L. J. Cote, J. Kim, V. C. Tung, J. Luo, F. Kim and J. Huang, *Pure Appl. Chem.*, 2010, **83**, 95-110.
57. L. Qiu, J. Z. Liu, S. L. Chang, Y. Wu and D. Li, *Nature Commun.*, 2012, **3**, 1241.
60. J. Tian, R. Ning, Q. Liu, A. M. Asiri, A. O. Al-Youbi and X. Sun, *ACS Appl. Mater. Interfaces*, 2014, **6**, 1011-1017.
61. K. Qiu and Z. X. Guo, *J. Mater. Chem.*, 2014, **2**, 3209.

Nanoscale Accepted Manuscript